

Supporting Information

Installing Active Metal Species in Covalent Triazine Framework for Highly Efficient and Selective Photocatalytic CO₂ Reduction

Yiqing Jiang,^a Liangliang Xiong,^a Shien Guo,^{b,} Chao Xu,^a Jiaxin Wang,^a Xiaomin Wu,^a Yuting Xiao,^{a,*} Renjie Song^{a,*}*

^aKey Laboratory of Jiangxi Province for Persistent Pollutants Control and Resources Recycle, Nanchang Hangkong University, Nanchang 330063, Republic of China; Email: yutingxiao9@sina.com, srj0731@hnu.edu.cn

^bSchool of Chemical Engineering, Jiangxi Normal University, Nanchang 330022, People's Republic of China; Email: guoshien@jxnu.edu.cn

Contents

Materials	S3
Characterization.....	S3
DFT calculation	S3
Fig. S1. FT-IR spectra of TAPT and DP.	S5
Fig. S2. Solid-state ^{13}C MAS NMR spectra of PT-CTF.....	S5
Fig. S3. XRD patterns of PT-CTF, Co-PT-CTF, Ni-PT-CTF, and Zn-PT-CTF.	S6
Fig. S4. N_2 adsorption-desorption isotherms and corresponding pore size distribution plots (inset) of (a) PT-CTF, (b) Co-PT-CTF, (c) Ni-PT-CTF, and (d) Zn-PT-CTF.....	S7
Table S1. Summary of BET surface areas and pore volumes of PT-CTF and M-PT-CTF samples.	S7
Fig. S5. TGA curves of PT-CTF, Co-PT-CTF, Ni-PT-CTF and Zn-PT-CTF under a N_2 atmosphere.	S8
Fig. S6. XPS survey spectra of PT-CTF, Co-PT-CTF, Ni-PT-CTF and Zn-PT-CTF.	S8
Fig. S7. High resolution N 1s spectra of (a) PT-CTF, (b) Co-PT-CTF, (c) Ni-PT-CTF and, (d) Zn-PT-CTF.	S9
Fig. S8. SEM images of (a) PT-CTF, (b) Co-PT-CTF, (c) Ni-PT-CTF, and (d) Zn-PT-CTF.	S10
Fig. S9. TEM image and corresponding EDX elemental mapping images of Co-PT-CTF.	S11
Fig. S10. TEM image and corresponding EDX elemental mapping images of Zn-PT-CTF.	S11
Fig. S11. DOS plots for (a) PT-CTF, (b) Co-PT-CTF, (c)Ni-PT-CTF and (d) Zn-PT-CTF.....	S12
Fig. S12. VB-XPS spectra for (a) PT-CTF, (b) Co-PT-CTF, (c) Ni-PT-CTF and (d) Zn-PT-CTF.	S13
Fig. S13. Time course of (a) CO, and (b) H_2 production amounts under the irradiation of visible light over different as-prepared samples.....	S14
Fig. S14. ^1H -NMR spectra of the residual liquid obtained from CO_2 photoreduction for Ni-PT-CTF, d ⁶ -DMSO was used as the internal standard.....	S14
Fig. S15. Gas chromatography spectra of photocatalytic reduction products with $^{13}\text{CO}_2$ as a carbon source over Ni-PT-CTF.	S15
Table S2. Comparison of the activity of Ni-PT-CTF in the photocatalytic CO_2 reduction with the catalysts reported in literature.....	S16
Fig. S16. XRD patterns of Ni-PT-CTF before and after the cycling tests.....	S18
Fig. S17. FT-IR spectra of Ni-PT-CTF before and after recycling experiment.	S18
Fig. S19. TEM images of Ni-PT-CTF (a) before and (b) after recycling experiment.....	S20
Fig. S20. DFT-derived CO_2 binding structures for (a) PT-CTF, (b) Co-PT-CTF, (c) Ni-PT-CTF and, (d) Zn-PT-CTF.....	S20
Table S3. Fitted parameters from time-resolved PL spectra of pristine PT-CTF, Co-PT-CTF, Ni-PT-CTF and Zn-PT-CTF, respectively.....	S21
Fig. S21. Differential charge density of (a) PT-CTF, (b) Co-PT-CTF, (c)Ni-PT-CTF and (d) Zn-PT-CTF, where the isosurface value is 0.002 e \AA^{-3} , and yellow and cyan regions denote charge accumulation and depletion, respectively.....	S21
Fig. S22. The possible photoreaction pathways over the Ni-PT-CTF.....	S22

Materials

2,9-diformyl-1,10-phenanthroline, 2,4,6-tris (4-aminophenyl)-1,3,5-triazine, N,N-dimethylformamide, ethanol, 1,4-dioxane, methanol, CH₃CN, triethanolamine were received from Aladdin industrial Inc. and used without further purification.

Characterization

The X-ray diffraction (XRD) patterns of the samples were obtained on a Bruker D8 Advance diffractometer with Cu K α radiation (40 kV) at a scanning rate of 5° min⁻¹, ranging from 5° to 60°. Using a field emission scanning electron microscope (FESEM) (Nova Nanosem 200), the system was used to obtain images of the sample at an acceleration voltage of 20 kV. The morphology and microstructure of the materials were observed by transmission electron microscopy (TEM) and high-resolution transmission electron microscopy (HRTEM) on the JEOL-2100F instrument. Steady-state photoluminescence spectra and transient photoluminescence attenuation curves were obtained on the HORIBA FlouoroMax-4 fluorescence spectrometer. Ultraviolet-visible (UV-VIS) diffuse reflectance spectra are obtained on a spectrophotometer (Shimazu UV3600IPLUS). Fourier transform infrared spectroscopy was recorded in the Nicolet6700 infrared spectrometer. X-ray photoelectron spectroscopy (XPS) analysis at AXIS SUPRA, Shimadzu. The binding energy of C 1s (284.8eV) was used to calibrate the binding energy. Nitrogen adsorption-desorption curves characterizing the specific surface area and pore size distribution of BET (Brunauer-Emmett-Teller) were obtained in the Micromeritics ASAP 2010 system, and CO₂ adsorption-desorption curves were also obtained.

DFT calculation

All the DFT calculations were conducted based on the Vienna Ab initio Simulation Package (VASP).^[1,2] The exchange-correlation potential was described by the Perdew-Burke-Ernzerhof (PBE) generalized gradient approach (GGA).^[3] The electron-ion interactions were accounted by the projector augmented wave (PAW).^[4] All DFT calculations were performed with a cut-off energy of 400 eV, and the Brillouin zone

was sampled using with the gamma (Γ) K-point. The energy and force convergence criteria of the self-consistent iteration were set to 10^{-4} eV and 0.02 eV \AA^{-1} , respectively. DFT-D3 method was used to describe van der Waals (vdW) interactions.^[5]

The adsorption energies of CO₂ on the different surfaces were calculated according to the below equations:

$$E_{*CO_2} = E_{\text{tot}} - E_{\text{slab}} - E_{CO_2(g)}$$

E_{tot} and E_{slab} are the total energies of surface with and without species adsorption, $E_{CO_2(g)}$ are the energy of gas phase.

The Gibbs free energy changes (ΔG) of the reaction are calculated using the following formula:

$$\Delta G = \Delta E + \Delta ZPE - T \Delta S + \Delta G_U + \Delta G_{\text{pH}}$$

where ΔE is the difference of electron energies calculated by DFT; ΔZPE and ΔS are the changes of zero-point energy and entropy, respectively, which are obtained from vibrational frequencies. T is the temperature (298.15 K). $\Delta G_U = -eU$, where U is the applied electrode potential. $\Delta G_{\text{pH}} = kBT \times \ln 10 \times \text{pH}$, where kB is the Boltzmann constant.

References

- [1] G. Kresse, J. Hafner, Ab Initio molecular Dynamics for Liquid Metals, *Phys. Rev. B* **47** (1993) 558-561.
- [2] G. Kresse, J. Hafner, Ab initio molecular-dynamics simulation of the liquid-metalamorphous-semiconductor transition in germanium, *Phys. Rev. B Condens. Matter Mater. Phys.* **49** (1994) 14251–14269.
- [3] J. P. Perdew, K. Burke, M. Ernzerhof, Generalized Gradient Approximation Made Simple. *Phys. Rev. Lett.* **77** (1996) 3865-3868.
- [4] G. Kresse, D. Joubert, From ultrasoft pseudopotentials to the projector augmentedwave method, *Phys. Rev. B Condens. Matter Mater. Phys.* **59** (1999) 1758–1775.

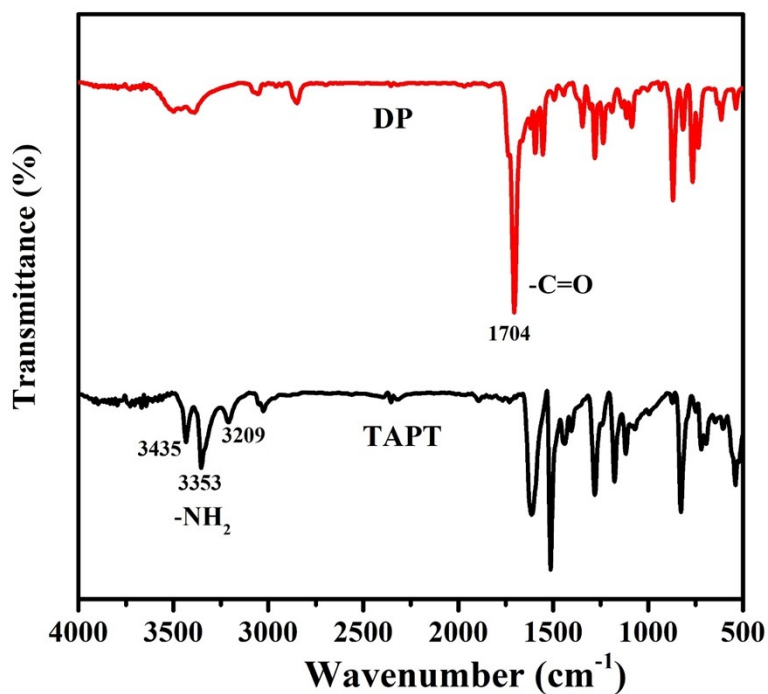


Fig. S1. FT-IR spectra of TAPT and DP.

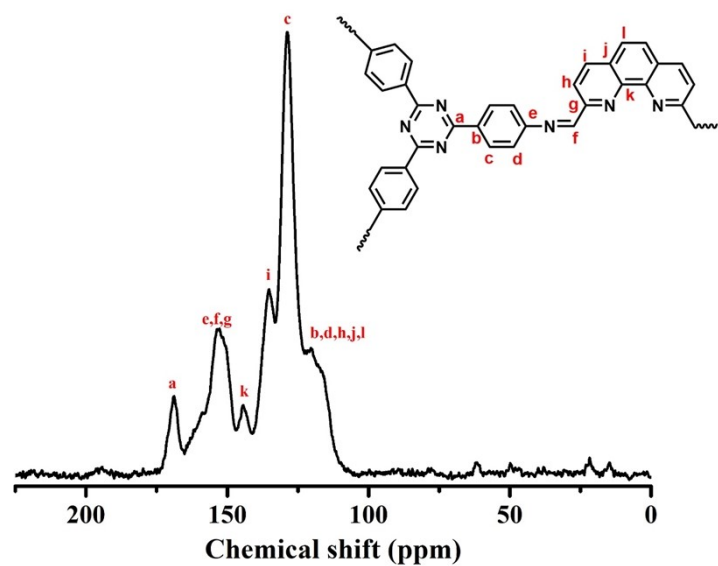


Fig. S2. Solid-state ¹³C MAS NMR spectra of PT-CTF.

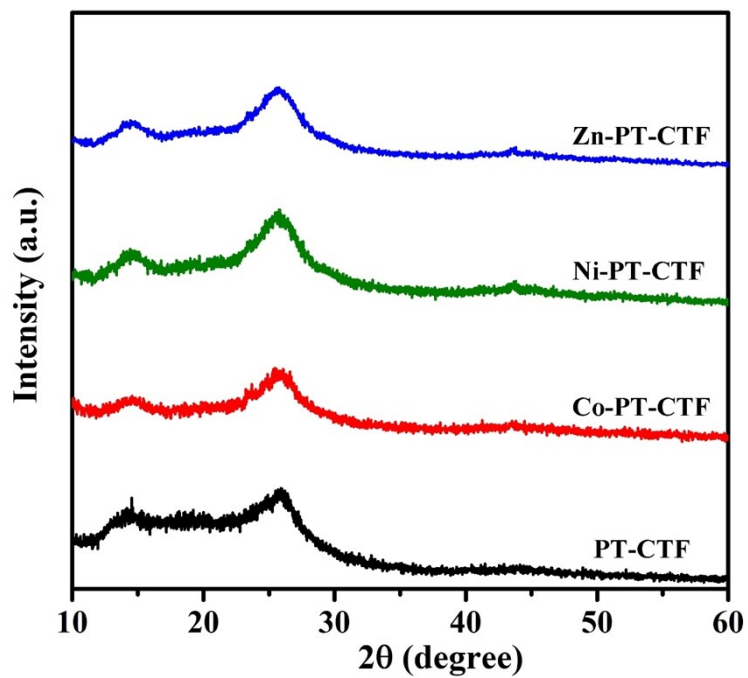


Fig. S3. XRD patterns of PT-CTF, Co-PT-CTF, Ni-PT-CTF, and Zn-PT-CTF.

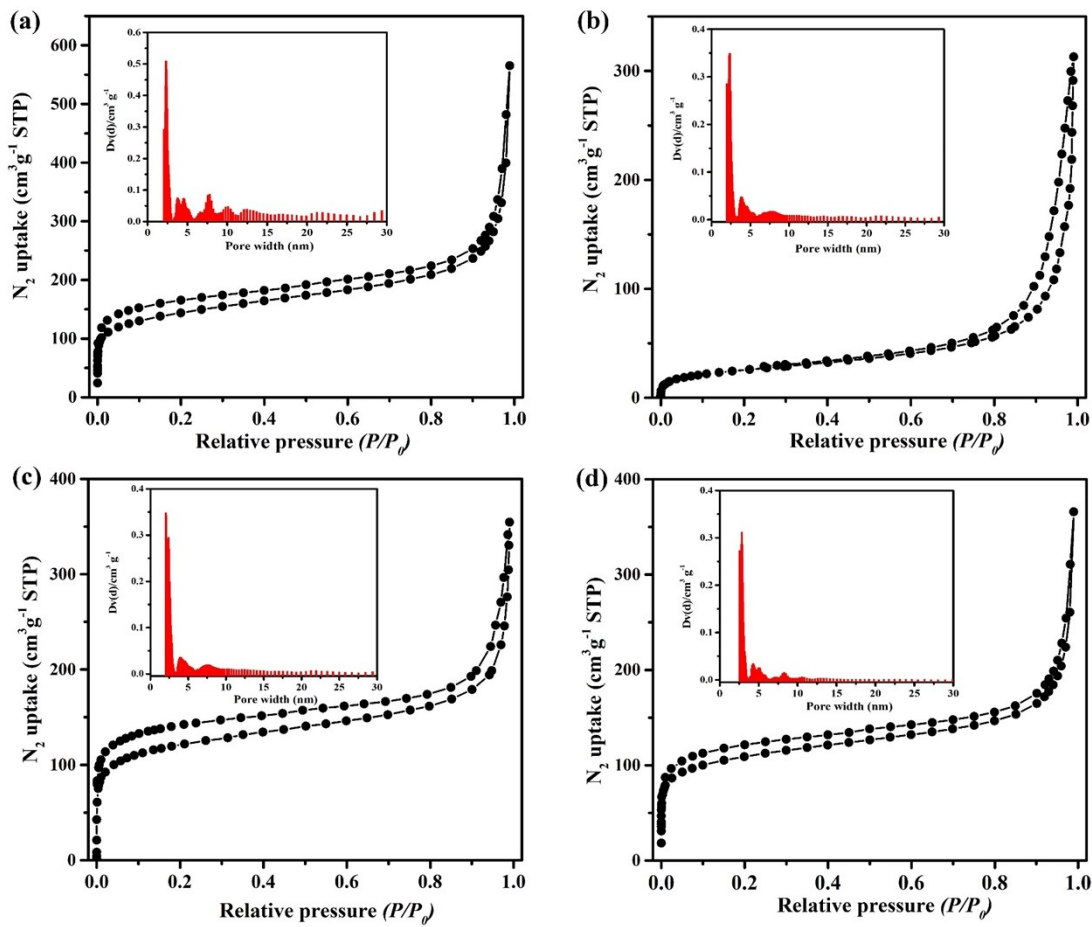


Fig. S4. N_2 adsorption-desorption isotherms and corresponding pore size distribution plots (inset) of (a) PT-CTF, (b) Co-PT-CTF, (c) Ni-PT-CTF, and (d) Zn-PT-CTF.

Table S1. Summary of BET surface areas and pore volumes of PT-CTF and M-PT-CTF samples.

Samples	BET surface areas (m^2/g)	Pore volume (cm^3/g)
PT-CTF	528.6	0.54
Co-PT-CTF	344.3	0.38
Ni-PT-CTF	398.7	0.41
Zn-PT-CTF	406.4	0.43

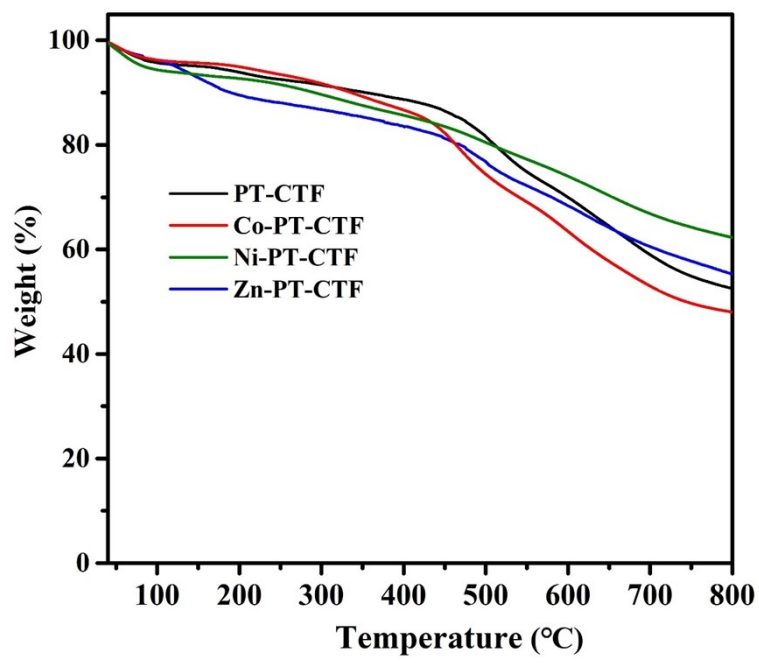


Fig. S5. TGA curves of PT-CTF, Co-PT-CTF, Ni-PT-CTF and Zn-PT-CTF under a N₂ atmosphere.

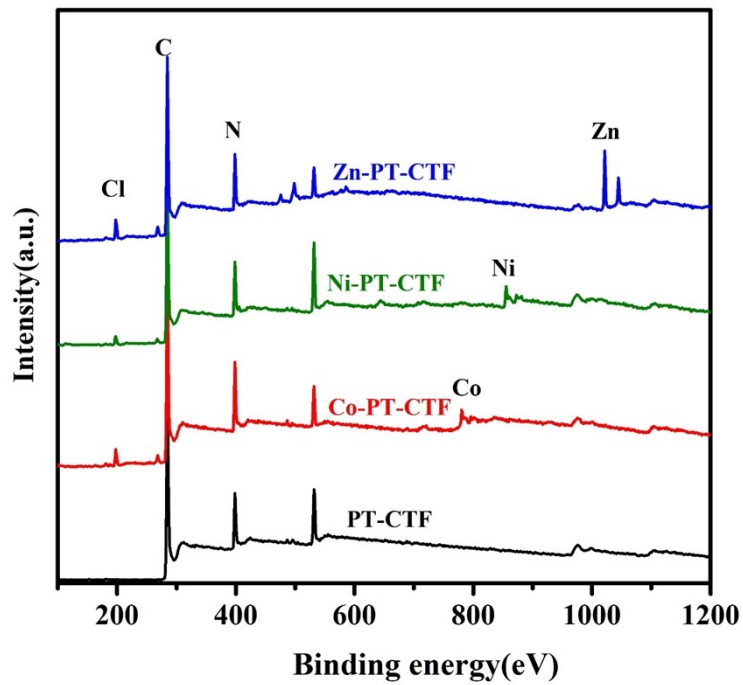


Fig. S6. XPS survey spectra of PT-CTF, Co-PT-CTF, Ni-PT-CTF and Zn-PT-CTF.

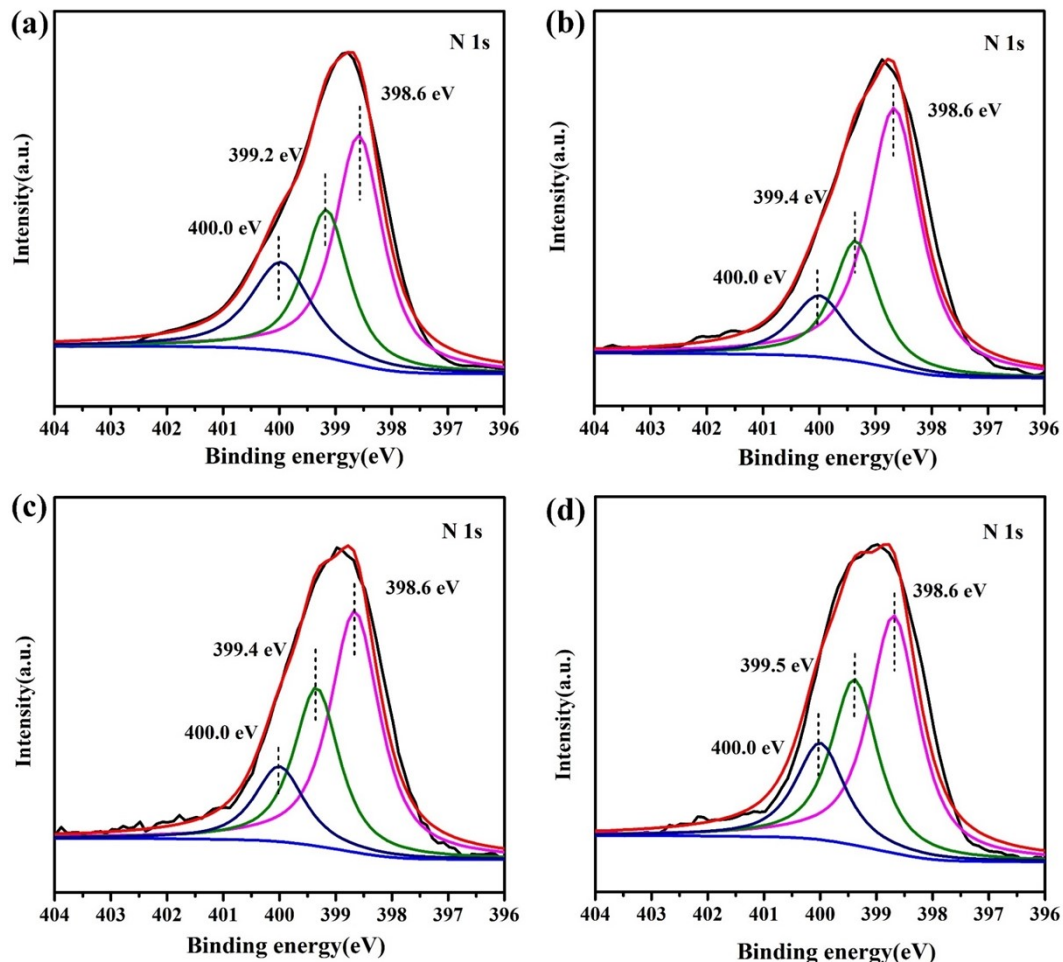


Fig. S7. High resolution N 1s spectra of (a) PT-CTF, (b) Co-PT-CTF, (c) Ni-PT-CTF and, (d) Zn-PT-CTF.

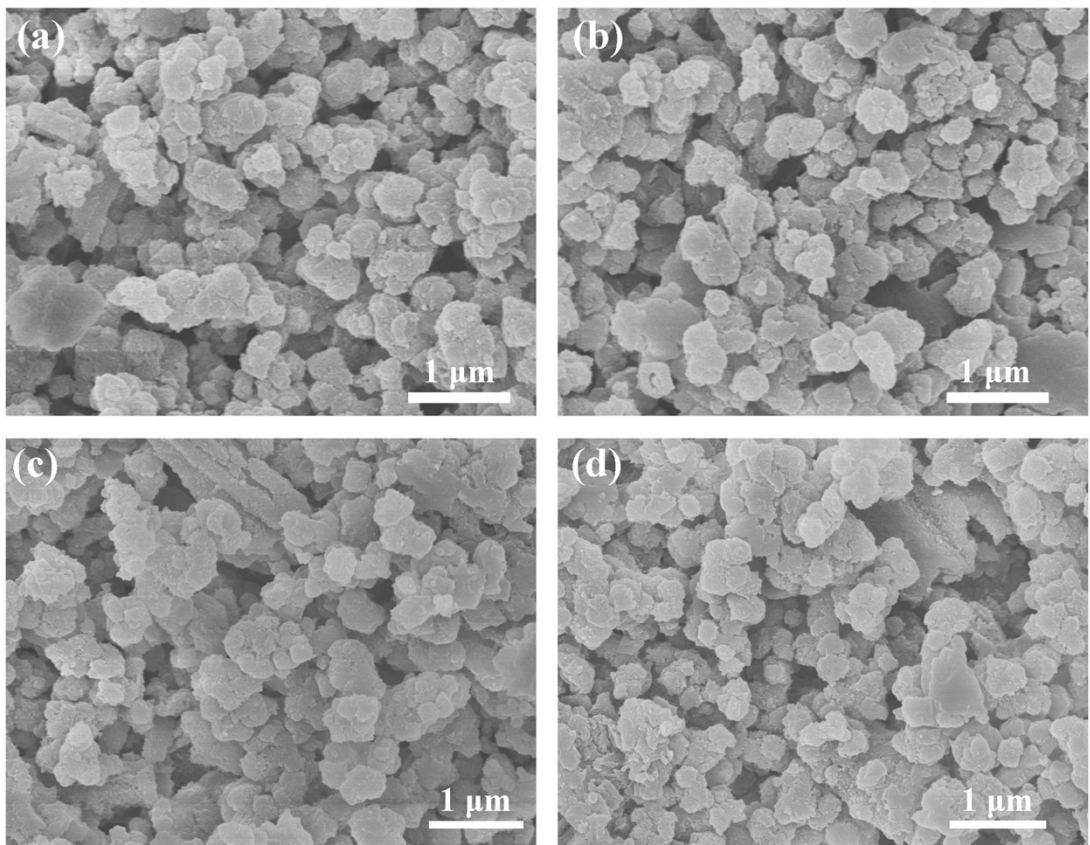


Fig. S8. SEM images of (a) PT-CTF, (b) Co-PT-CTF, (c) Ni-PT-CTF, and (d) Zn-PT-CTF.

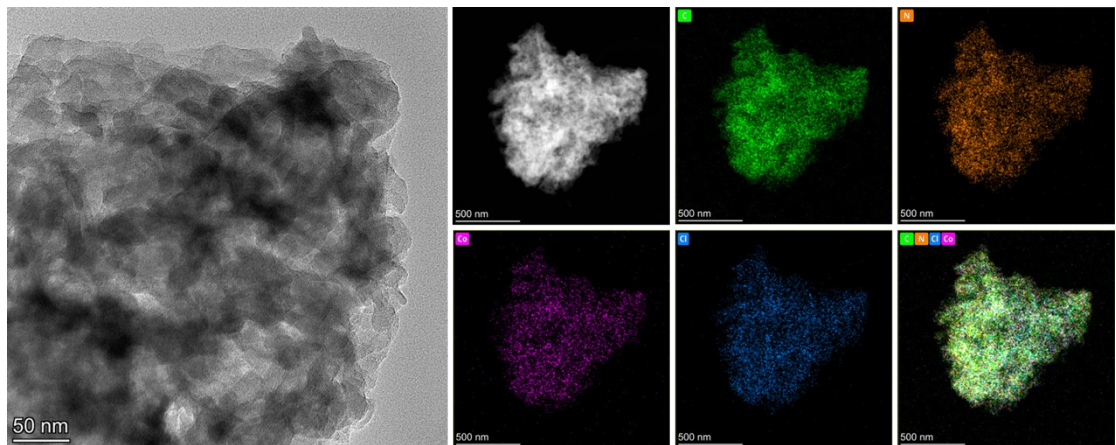


Fig. S9. TEM image and corresponding EDX elemental mapping images of Co-PT-CTF.

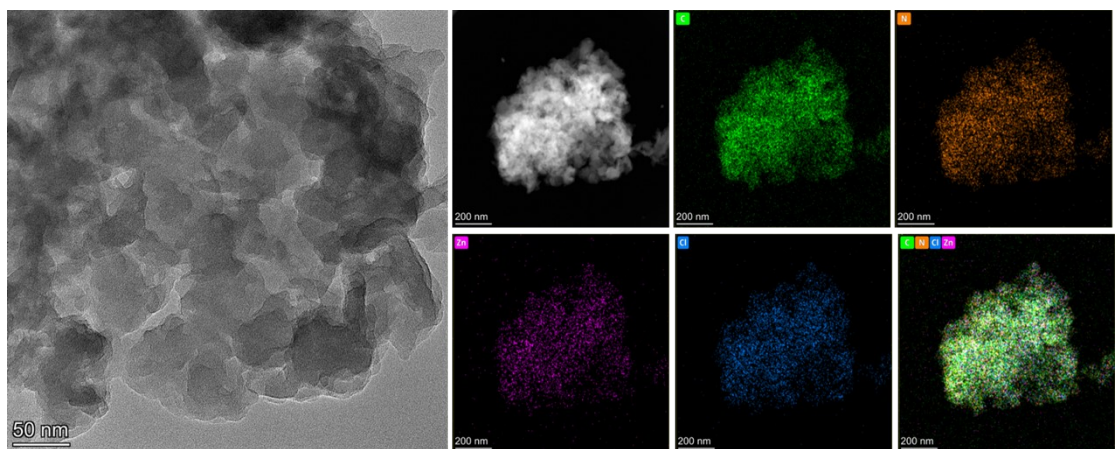


Fig. S10. TEM image and corresponding EDX elemental mapping images of Zn-PT-CTF.

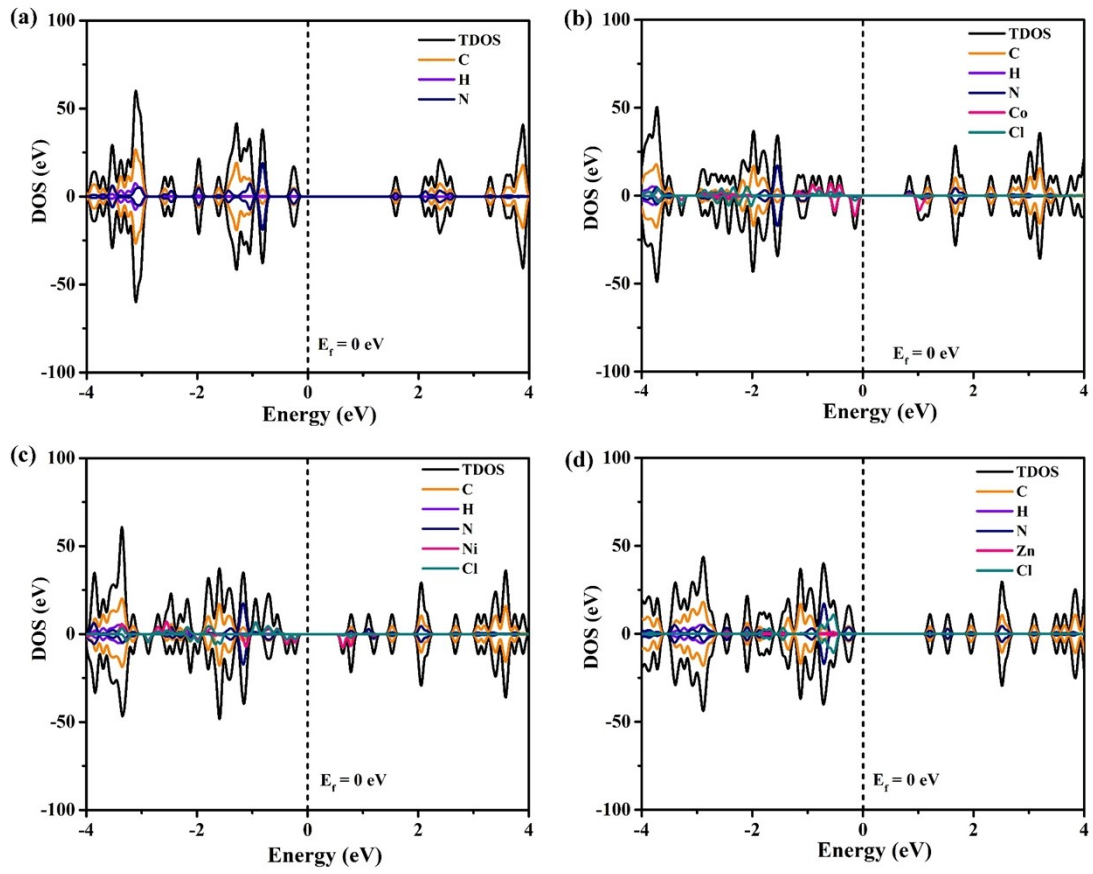


Fig. S11. DOS plots for (a) PT-CTF, (b) Co-PT-CTF, (c) Ni-PT-CTF and (d) Zn-PT-CTF.

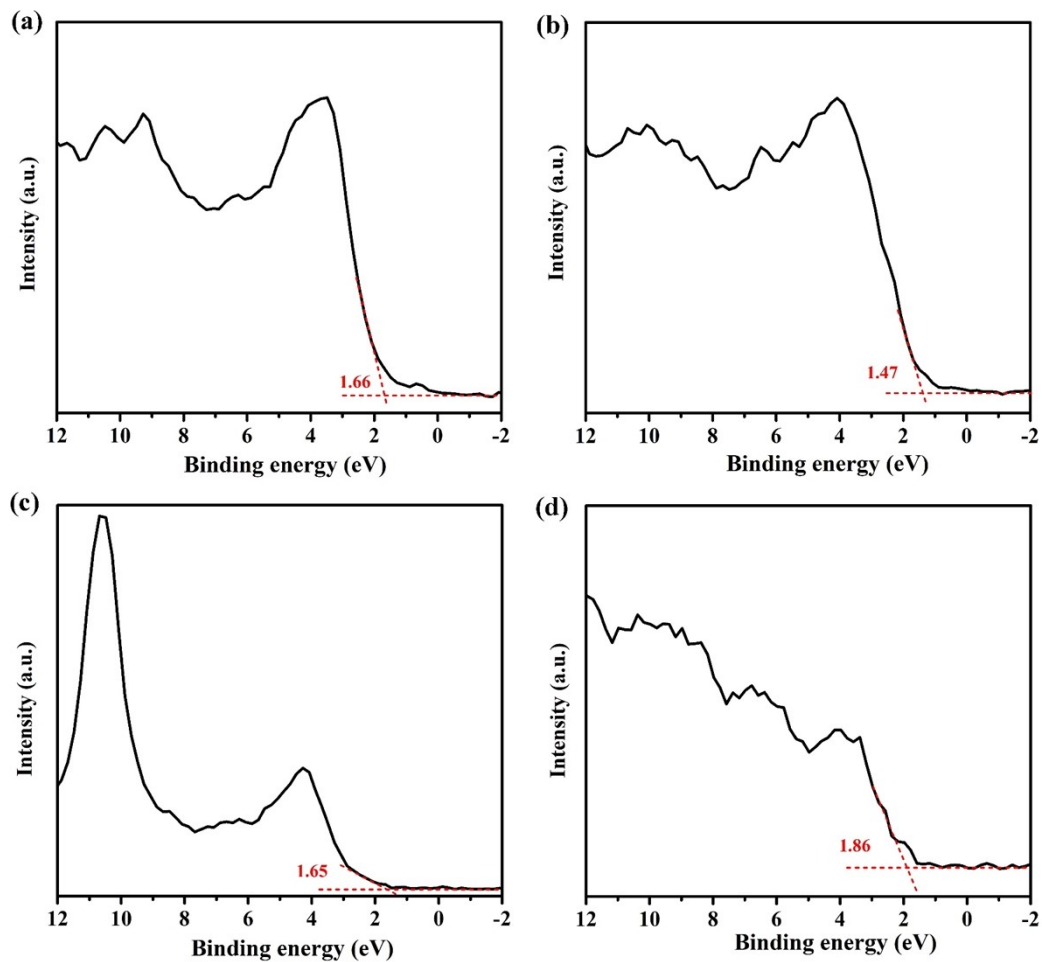


Fig. S12. VB-XPS spectra for (a) PT-CTF, (b) Co-PT-CTF, (c) Ni-PT-CTF and (d) Zn-PT-CTF.

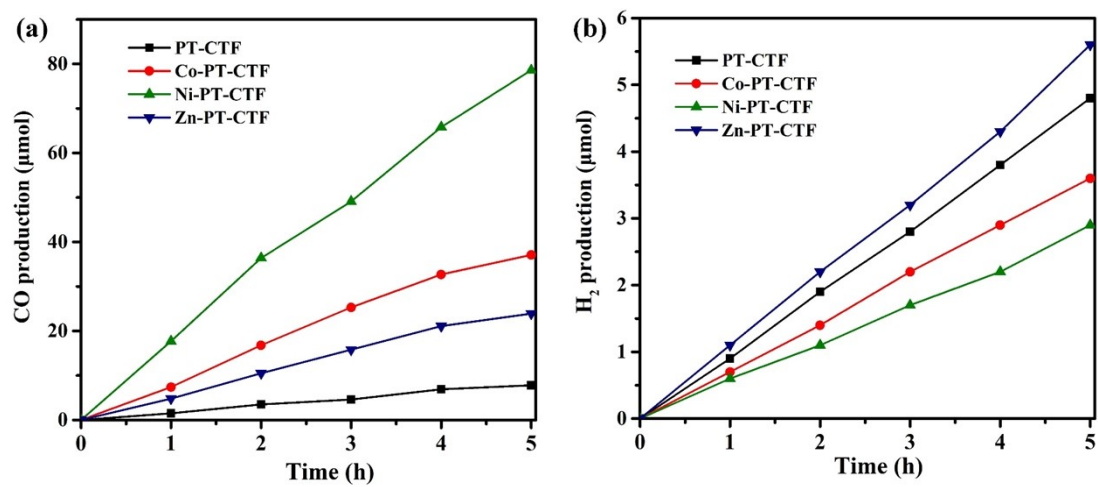


Fig. S13. Time course of (a) CO, and (b) H₂ production amounts under the irradiation of visible light over different as-prepared samples.

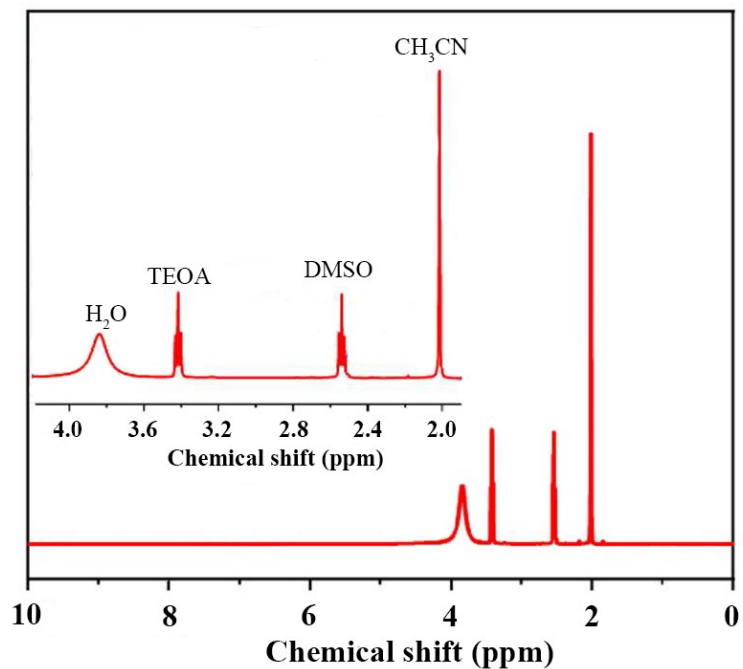


Fig. S14. ¹H-NMR spectra of the residual liquid obtained from CO₂ photoreduction for Ni-PT-CTF, d⁶-DMSO was used as the internal standard.

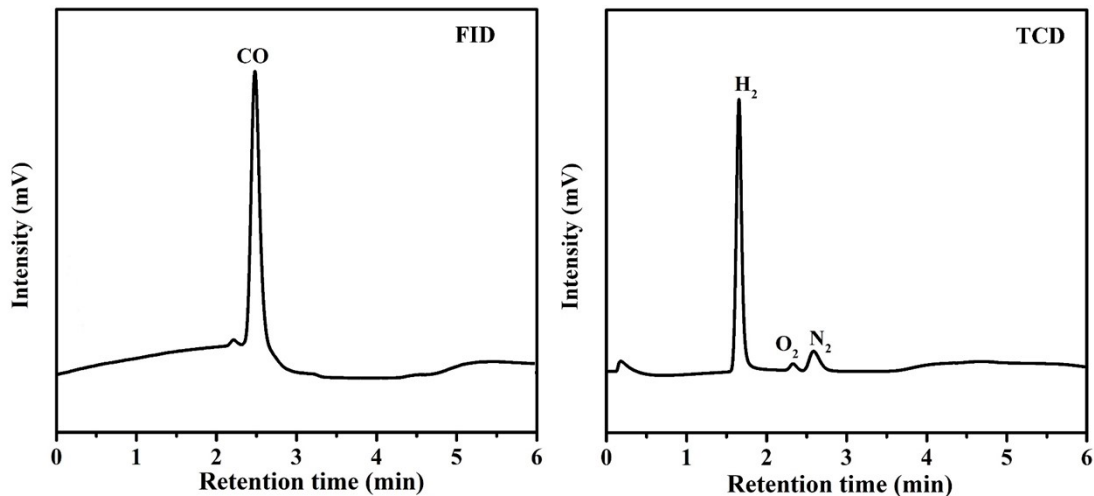


Fig. S15. Gas chromatography spectra of photocatalytic reduction products with $^{13}\text{CO}_2$ as a carbon source over Ni-PT-CTF.

Table S2. Comparison of the activity of Ni-PT-CTF in the photocatalytic CO₂ reduction with the catalysts reported in literature.

Sample	Reaction agent	Light source	Yield ($\mu\text{mol g}^{-1} \text{ h}^{-1}$)	Ref.
Re-CTF-py	MeCN/TEOA	Xe lamp $\lambda \geq 400 \text{ nm}$	CO: 353.05	[1]
Co/CTF-1	MeCN/TEOA/H ₂ O [Ru(bpy) ₃ Cl ₂]•6H ₂ O	Xe lamp $\lambda \geq 420 \text{ nm}$	CO: 50	[2]
CTF-TDPN	MeCN/TEOA/H ₂ O	Xe lamp $\lambda \geq 420 \text{ nm}$	CO: 330.3	[3]
Fe SAS/Tr-COF	MeCN/TEOA/H ₂ O [Ru(bpy) ₃ Cl ₂]•6H ₂ O	Xe lamp $\lambda \geq 420 \text{ nm}$	CO: 980.3	[4]
20%Ni-CTAB-CTF-1	MeCN/TEOA/H ₂ O [Ru(bpy) ₃ Cl ₂]•6H ₂ O	Xe lamp $\lambda > 420 \text{ nm}$	CO: 1254.15	[5]
SnS ₂ /S-CTF	TEOA/H ₂ O	Xe lamp $\lambda \geq 420 \text{ nm}$	CO: 123.6 CH ₄ : 43.4	[6]
Pd@Imine-CTF	TEOA/H ₂ O	Xe lamp $\lambda \geq 420 \text{ nm}$	CO: 85.3 CH ₄ : 21.1	[7]
Cs ₂ AgBiBr ₆ /CTF-1	EA	Xe lamp $\lambda \geq 420 \text{ nm}$	CO: 122.9	[8]
CsPbBr ₃ /CTF-1	EA	Xe lamp $\lambda \geq 400 \text{ nm}$	CO: 173	[9]
CN/CTF	MeCN/TEOA	Xe lamp $\lambda \geq 420 \text{ nm}$	CO: 151.1	[10]
Ni-PT-CTF	MeCN/TEOA/H ₂ O	Xe lamp $\lambda \geq 420 \text{ nm}$	CO: 784.5	This work

Reference

- [1] R. Xu, X.-S. Wang, H. Zhao, H. Lin, Y.-B. Huang, R. Cao, Rhenium-modified porous covalent triazine framework for highly efficient photocatalytic carbon dioxide

- reduction in a solid–gas system, *Catal. Sci. Technol.* 8 (2018) 2224-2230.
- [2] J. Bi, B. Xu, L. Sun, H. Huang, S. Fang, L. Li, L. Wu, A Cobalt-Modified Covalent Triazine-Based Framework as an Efficient Cocatalyst for Visible-Light-Driven Photocatalytic CO₂ Reduction, *ChemPlusChem* 84 (2019) 1149-1154.
- [3] Y. He, X. Chen, C. Huang, L. Li, C. Yang, Y. Yu, Encapsulation of Co single sites in covalent triazine frameworks for photocatalytic production of syngas, *Chinese J. Catal.* 42 (2021) 123-130.
- [4] L. Ran, Z. Li, B. Ran, J. Cao, Y. Zhao, T. Shao, Y. Song, M.K.H. Leung, L. Sun, J. Hou, Engineering Single-Atom Active Sites on Covalent Organic Frameworks for Boosting CO₂ Photoreduction, *J. Am. Chem. Soc.* 144 (2022) 17097-17109.
- [5] J. Tian, J. Zhang, B. Xu, Q. Chen, G. Huang, J. Bi, An Artificial Photosystem of Metal-Insulator-CTF Nanoarchitectures for Highly Efficient and Selective CO₂ Conversion to CO, *ChemSusChem* 15 (2022) e202201107.
- [6] S. Guo, P. Yang, Y. Zhao, X. Yu, Y. Wu, H. Zhang, B. Yu, B. Han, M.W. George, Z. Liu, Direct Z-Scheme Heterojunction of SnS₂/Sulfur-Bridged Covalent Triazine Frameworks for Visible-Light-Driven CO₂ Photoreduction, *ChemSusChem* 13 (2020) 6278-6283.
- [7] S. Guo, Y. Xiao, B. Jiang, Encapsulation of Pd Nanoparticles in Covalent Triazine Frameworks for Enhanced Photocatalytic CO₂ Conversion, *ACS Sustain. Chem. Eng.* 9 (2021) 12646-12654.
- [8] Z. Zhang, Y. Jiang, Z. Dong, Y. Chu, J. Xu, 2D/2D Inorganic/Organic Hybrid of Lead-Free Cs₂AgBiBr₆ Double Perovskite/Covalent Triazine Frameworks with Boosted Charge Separation and Efficient CO₂ Photoreduction, *Inorg. Chem.* 61 (2022) 16028-16037.
- [9] Q. Wang, J. Wang, J.-C. Wang, X. Hu, Y. Bai, X. Zhong, Z. Li, Coupling CsPbBr₃ Quantum Dots with Covalent Triazine Frameworks for Visible-Light-Driven CO₂ Reduction, *ChemSusChem* 14 (2021) 1131-1139.
- [10] J. He, X. Wang, S. Jin, Z.-Q. Liu, M. Zhu, 2D metal-free heterostructure of covalent triazine framework/g-C₃N₄ for enhanced photocatalytic CO₂ reduction with high selectivity, *Chinese J. Catal.* 43 (2022) 1306-1315.

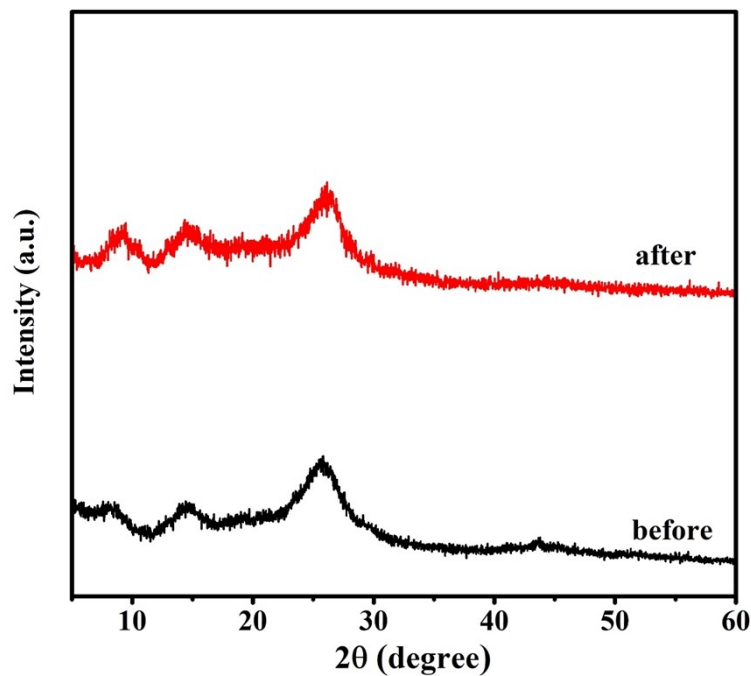


Fig. S16. XRD patterns of Ni-PT-CTF before and after the cycling tests.

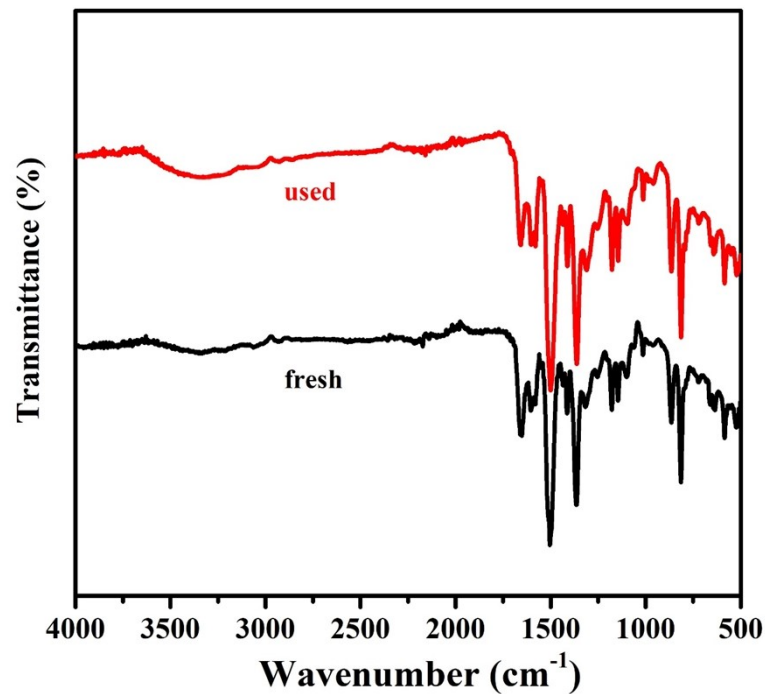


Fig. S17. FT-IR spectra of Ni-PT-CTF before and after recycling experiment.

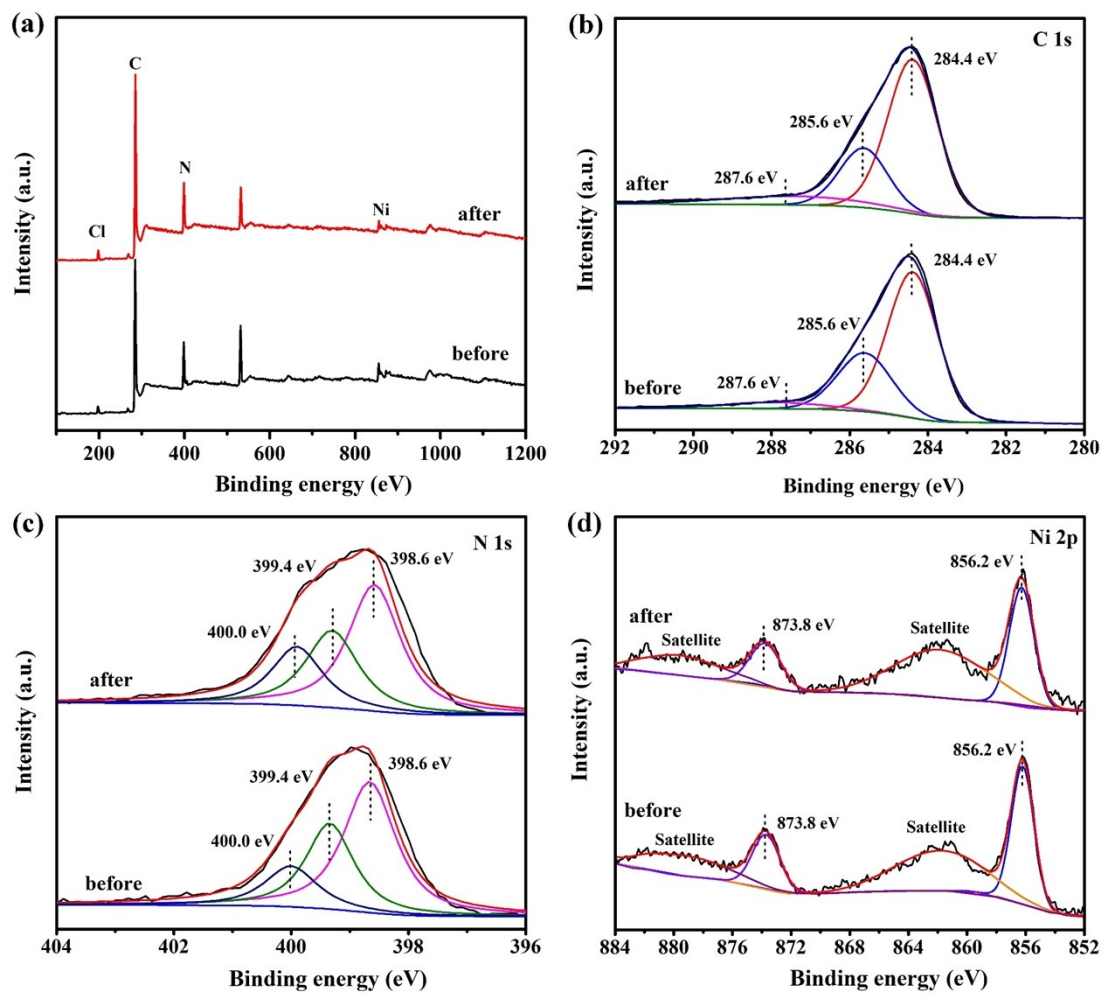


Fig. S18. XPS spectra of Ni-PT-CTF before and after the cycling tests. Full spectra (a), high-resolution (b) C 1s, (c) N 1s and (d) Ni 2p.

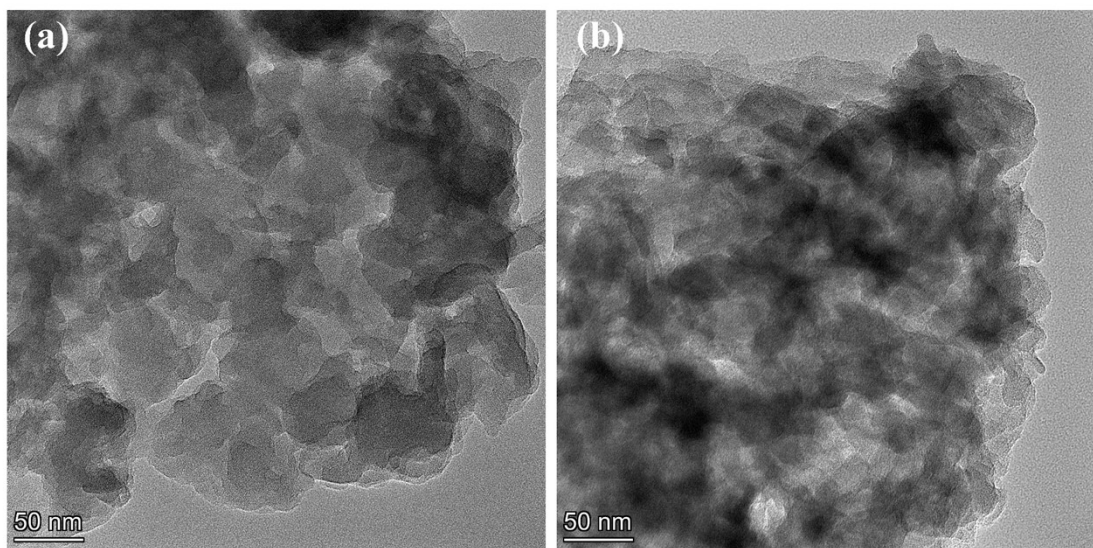


Fig. S19. TEM images of Ni-PT-CTF (a) before and (b) after recycling experiment.

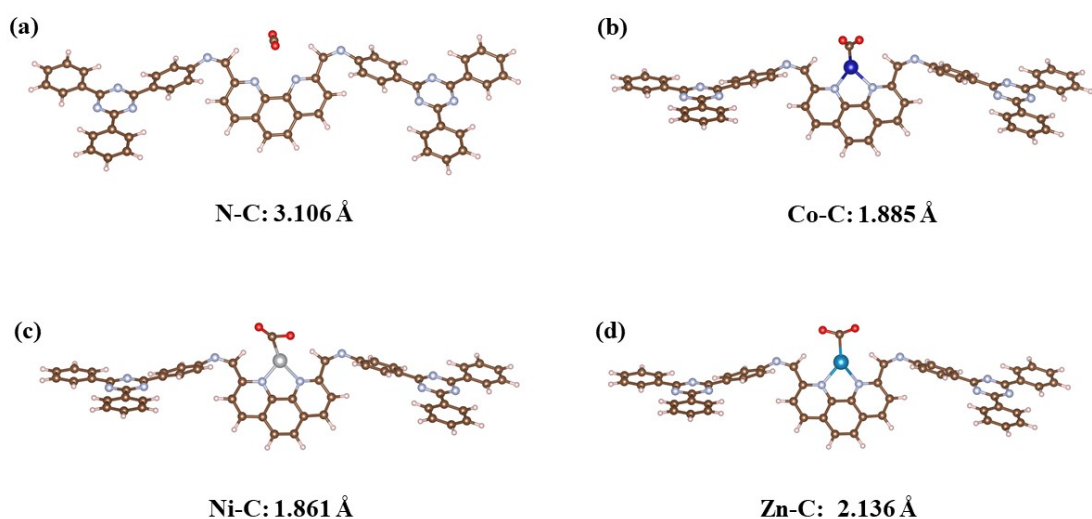


Fig. S20. DFT-derived CO_2 binding structures for (a) PT-CTF, (b) Co-PT-CTF, (c) Ni-PT-CTF and, (d) Zn-PT-CTF.

Table S3. Fitted parameters from time-resolved PL spectra of pristine PT-CTF, Co-PT-CTF, Ni-PT-CTF and Zn-PT-CTF, respectively.

Photocatalysts	τ_1	Rel.%	τ_2	Rel.%	τ
PT-CTF	0.40	69.48	5.01	30.52	4.30
Co-PT-CTF	1.68	34.88	8.98	65.12	8.31
Ni-PT-CTF	1.82	31.29	9.85	68.71	9.23
Zn-PT-CTF	0.75	39.72	7.35	60.28	6.93

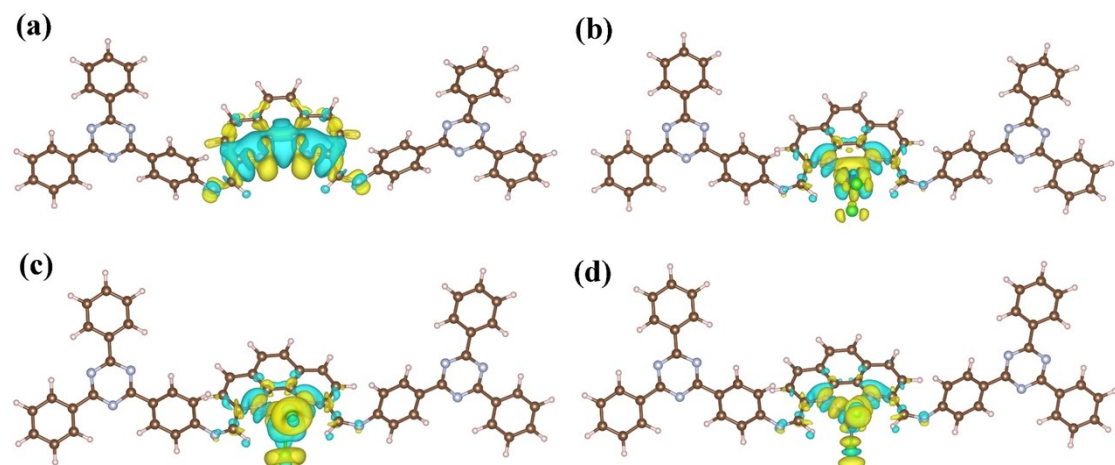
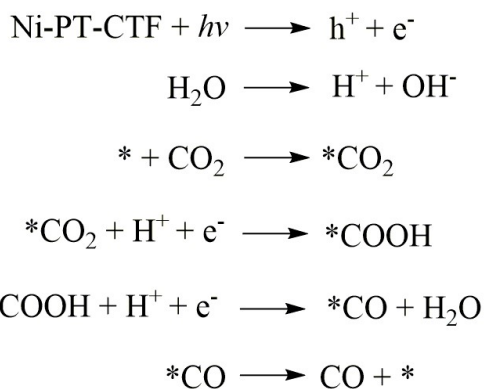


Fig. S21. Differential charge density of (a) PT-CTF, (b) Co-PT-CTF, (c) Ni-PT-CTF and (d) Zn-PT-CTF, where the isosurface value is $0.002 \text{ e } \text{\AA}^{-3}$, and yellow and cyan regions denote charge accumulation and depletion, respectively.

Reduction pathway



where * stands catalytically active site during the photocatalytic CO_2 reduction process.

Fig. S22. The possible photoreaction pathways over the Ni-PT-CTF.